Materials Characterization 200 (2023) 112886

Contents lists available at ScienceDirect

Materials Characterization

journal homepage: www.elsevier.com/locate/matchar

Controlled precipitation in a new Al-Mg-Sc alloy for enhanced corrosion behavior while maintaining the mechanical performance

Sanjay C. Krishnamurthy [a], Mariia Arseenko [a], Ankush Kashiwar [a,b], Philippe Dufour [c], Yves Marchal [c], Jocelyn Delahaye [d], Hosni Idrissi [a,b], Thomas Pardoen [a], Anne Mertens [d], Aude Simar [a,*]

[a] Université catholique de Louvain, Institute of Mechanics, Materials and Civil Engineering (iMMC), IMAP, Place Sainte Barbe 2, B-1348 Louvain-la-Neuve, Belgium
[b] Department of Physics, Electron Microscopy for Materials Science (EMAT), University of Antwerp, Groenenborgerlaan 171, B-2020 Antwerpen, Belgium
[c] SONACA, Gosselies, Belgium
[d] Université de Liège, Aerospace and Mechanics Department, Metallic Materials Science, Allée de la Découverte 13A, Quartier Polytech 1, B-4000 Liège, Belgium

ARTICLE INFO

Keywords:
Al-Mg-Sc alloy
Cooling rate
Inter granular corrosion
Precipitation

ABSTRACT

The hot working of 5xxx series alloys with Mg ≥3.5 wt% is a concern due to the precipitation of β (Al_3Mg_2) phase at grain boundaries favoring Inter Granular Corrosion (IGC). The mechanical and corrosion properties of a new 5028-H116 Al-Mg-Sc alloy under various β precipitates distribution is analyzed by imposing different cooling rates from the hot forming temperature (i.e. 325 °C). The mechanical properties are maintained regardless of the heat treatment. However, the different nucleation sites and volume fractions of β precipitates for different cooling rates critically affect IGC. Controlled furnace cooling after the 325 °C heat treatment is ideal in 5028-H116 alloy to reduce susceptibility to IGC after sensitization.

1. Introduction

The application of 5xxx series aluminum alloy as structural components in aerospace industry has gained renewed interest following the addition of scandium as micro-alloying element [1,2]. The Al-Mg-Sc alloys have excellent toughness and damage tolerance along with superior corrosion resistance compared to conventional aerospace alloys [1]. Processing Al-Mg-Sc sheets by hot creep forming has gained immense interest in aerospace industry due to the above mentioned properties and absence of spring back effect [3,4]. Recently 5028-H116 commercial Al-Mg-Sc alloy sheets have been made available for aerospace applications. Due to its very low density and good mechanical properties, it is a prospective candidate for replacement of many existing Al alloys in industry [5].

The main drawback of aluminum-magnesium alloys with Mg ≥3.5 wt% is the susceptibility to inter-granular corrosion (IGC) when subjected to heating (50°-220 °C) [6]. This susceptibility is due to the precipitation of β (Al_3Mg_2) phase at grain boundaries. The general precipitation sequence in Al-Mg alloys is SSSS (supersaturated solid solution) → GP (Guinier Preston) zones → β'' (Al_3Mg_2) → β' (Al_3Mg_2) → β (Al_3Mg_2) [7–9]. In Al-Mg alloys with a Mg content below 18 wt%, GP zones and β'' precipitates are only rarely reported. However, the metastable β' and equilibrium β precipitates are the most frequent primary phases observed in low Mg content (<13 wt%) Al alloys, which is the case for 5028 alloy [7–9].

The β phase precipitates heterogeneously at grain boundaries (GB), at triple junctions or on pre-existing Mn dispersoids [6,10]. The GB nucleation sites in Al-Mg alloys are dependent on the GB misorientation [11]. In addition, the dislocation density, type of dispersoids and their density, and the processing temperature also influence precipitation [8,12,13]. The diffusion rate of Mg is found to be high in the presence of high dislocation density in Al-Mg alloys [14]. H116 temper rolling is widely accepted as being a corrosion resistant temper in Al-Mg alloys. To the best of our knowledge no detailed studies determine and quantitatively compare the nucleation sites of β phase precipitates formed in heat treated wrought Al-Mg alloys.

The electrochemical potential of β (Al_3Mg_2) phase is −1.013 V while it is −0.823 V for Al [15]. Thus, Intergranular corrosion (IGC) occurs due to the anodic corrosion of β (Al_3Mg_2) phase precipitate at the GB [6]. Zhang et al. [6] summarized the effect of temperature and time on the degree of sensitization (DOS) of various 5xxx series alloys. Here, sensitization refers to the precipitation of β (Al_3Mg_2) phase when subjected to

* Corresponding author at: Place Sainte-Barbe 2, L5.02.02 Louvain-la-Neuve, 1348, Belgium.
E-mail address: aude.simar@uclouvain.be (A. Simar).

https://doi.org/10.1016/j.matchar.2023.112886
Received 26 November 2022; Received in revised form 5 March 2023; Accepted 31 March 2023
Available online 3 April 2023

Table 1
AR 5028-H116 alloy chemical composition in wt%. (rest Al content).

Element	Si	Fe	Cu	Mn	Mg	Cr	Zn	Ti	Zr	Sc
Wt%	0.0–0.3	0.0–0.4	0.0–0.2	0.3–1.0	**3.2–4.8**	0.05–0.15	0.05–0.50	0.05–0.15	0.05–0.15	**0.02–0.40**

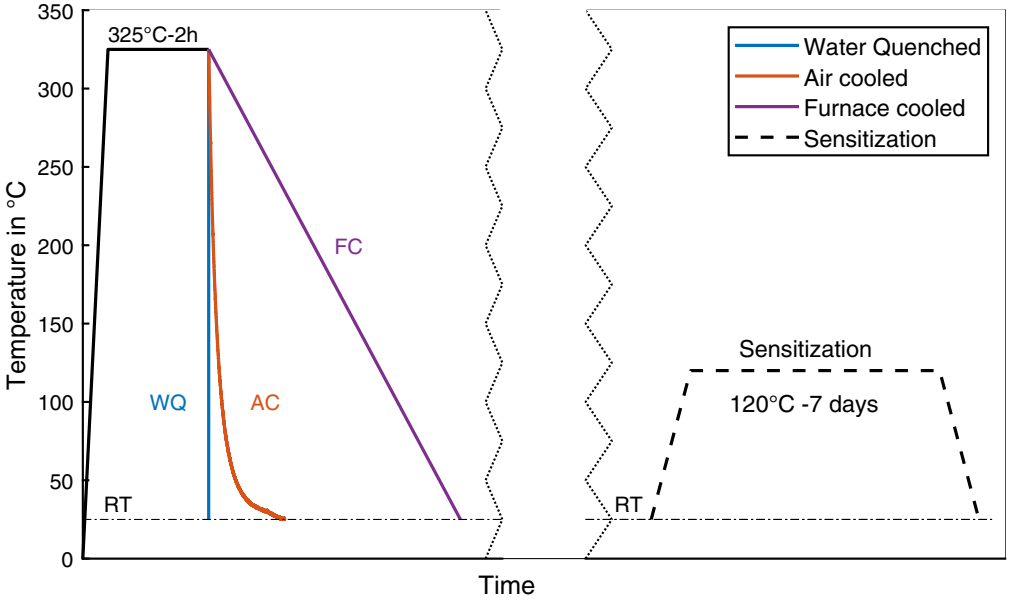

Fig. 1. Schematic of the heat treatment and cooling rate applied on AR 5028-H116 aluminum alloy (RT = Room Temperature).

moderate temperature (50–220 °C) for an extended duration [6]. Gaosong et al. [10] showed that continuous β phase precipitates favor IGC compared to thicker but discontinuous β precipitate at GB in 5456-H116 aluminum alloy. Wu et al. [16] also showed that discontinuous β phase precipitation causes a reduction in corrosion rate in Al-4.6 Mg(Mn,Zn) alloy. Zhang et al. [17] analyzed the DOS of 5083 alloy comparing various processing methods. They showed that the dominant effect favoring IGC was the grain size (with sub-micrometer grains) compared to GB misorientation.

Usual 5xxx series aluminum alloys are strengthened by solid solution hardening and cold working (strain hardening). Thus, the depletion of Mg in the matrix significantly deteriorates the strength when heat treated and sensitized at temperature 50–220 °C, again due to the β phase precipitation [18]. Recent studies have made the 5xxx series alloys heat treatable using Sc as micro-alloying element [19,20]. Limited addition of Sc causes a significant increase of the Al-Mg alloys strength [21]. Sc has also been reported to favor grain refinement in aluminum alloys [20]. Several studies have shown that a thermal treatment of Al-Mg-Sc alloy at 250–350 °C leads to a strength increase due to the formation of Al_3Sc precipitates that pin dislocations [22,23]. Kendig et al. [24] found that the major strengthening effect in Al-Mg-Sc alloy is from the sub-micron grains, followed by Al_3Sc particles and lastly solid solution strengthening of Mg. These Al_3Sc are highly stable with heat treatment and thus the strength of Al-Mg-Sc alloys is retained after heat treatments. This is due to the Zener drag effect which pins dislocations and grain boundaries, also inhibiting recovery and recrystallization [25].

The Al-Mg alloy with Sc addition has shown better corrosion resistance post sensitization at 130 °C for 168 h compared to the alloy without Sc [21]. The mechanical properties after sensitization are still not known. In general, the sensitization of Al-Mg-Sc alloy on mechanical and corrosion properties has rarely been reported [21,26]. Wu et al. [16] showed that annealing Al-Mg alloy at 480 °C for 8 h increased corrosion resistance during sensitization at 160 °C for 3 days. This was attributed to the formation of intermittent β phase precipitates during cooling inside the furnace.

The objective of this work is to analyze the effect of the cooling rate on the corrosion behavior and mechanical properties of a newly developed Al alloy 5028-H116. The Mg wt% in this alloy lies in the limit of susceptibility to IGC, however, its corrosion resistance is barely reported in literature. In addition, the effect of the cooling rate after heat treatment on the Al-Mg-Sc alloy corrosion resistance but also on the mechanical properties is lacking in literature. Focus of this work is laid on the effect of some sensitization treatment applied after hot creep forming and cooling to simulate the in-service behavior of the alloy. The impact on mechanical and corrosion resistance is explained based on the analysis of the changes in the β (Al_3Mg_2) phase precipitation sites under different cooling conditions.

2. Materials and methods

The aluminum alloy considered in this study is the Al-Mg-Sc 5028 alloy with a sheet thickness of 4.7 mm. The as received (AR) 5028-H116 alloy has undergone cold rolling until H116 temper. The composition of the alloy is provided in Table 1.

The alloy AR 5028-H116 was annealed at 325 °C for 2 h. The annealing temperature and time are representative of creep forming thermal conditions [3]. Three different cooling rates were compared (see Fig. 1): Water Quenching (WQ) with water at room temperature, Air Cooling (AC) and controlled Furnace Cooling (FC). The WQ, AC and FC materials were additionally subjected to heat treatment at 120 °C for 7 days, which here is called “sensitization heat treatment”. Sensitized conditions are called: WQ+S, AC+S and FC+S.

The microstructure characterization was conducted using an Olympus optical microscope and ZEISS ULTRA-55 scanning electron microscope (SEM) equipped with energy dispersive X-Ray (EDX) system. Electron backscatter diffraction (EBSD) mapping was performed with a field emission gun SEM (SigmaTM, Zeiss) equipped with a Symmetry S2 EBSD detector.

Transmission electron microscopy (TEM) specimens were prepared

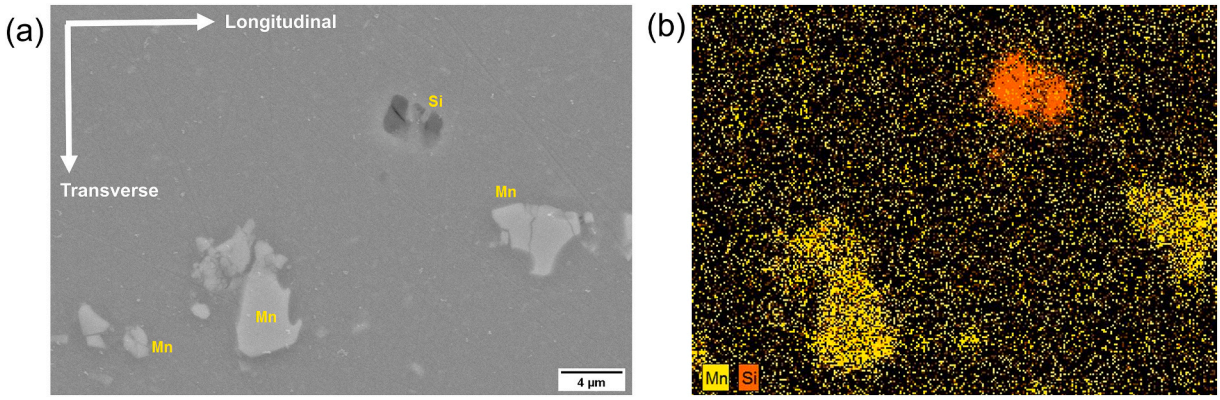

Fig. 2. (a) SEM micrograph of the as received (AR) 5028-H116 aluminum alloy providing an overview of the microstructure and (b) an EDX map of the microstructure identifying Mn and Si rich intermetallics.

by mechanical polishing followed by ion milling using Gatan Duo 691 precision ion polishing system (PIPS). STEM-EDX mapping and STEM high-angle annular dark-field detector (STEM-HAADF) images were acquired using a FEI Tecnai Osiris TEM operated at 200 kV and equipped with a highly efficient SuperX system. The post-treatment of the EDX data was carried using Bruker ESPRIT software. The statistical analysis of the β phase precipitates were computed using ImageJ software. Around 40–50 precipitates were considered under each condition for the quantitative analysis. The nearest neighbor distance (NND) was computed based on the distance between each β precipitate and its closest neighbor.

Differential scanning calorimetry (DSC) was performed with a Netzsch DSC 404 C Pegasus model equipment. The DSC samples were extracted from heat treated materials by micro-cutting. The weight of all the DSC samples was chosen to be ~40 mg, to obtain a good signal to noise ratio. The specimens were heated at a constant rate of 10 °C/min in argon atmosphere. The identification and analysis of the DSC curves and peaks were based on literature [7,27]. The baseline signal was subtracted from the DSC signal curves to identify the phase transition peaks. The area below these phase transition peaks indicates the enthalpy of formation/dissolution of the phase. Milkereit et al. [28] have shown that the precipitation enthalpy measured by DSC is directly proportional to the atomic or volume fraction of precipitates.

The Vickers micro-hardness testing was conducted under a load of 200 g with a dwell time of 15 s following ISO 6507-2:2018 [29] on an Emco-Test Durascan 5G equipment. The tensile test specimens were machined following ASTM E8 standard [30] (sub size specimen) with the tensile direction taken along the rolling direction. The tensile tests were performed on a Zwick 50 kN tensile machine with an extensometer throughout the test and loaded at a constant rate of 1 mm/min. The data acquisition frequency was set to 100 Hz. The extensometer gauge length was 20 mm. Four tests per condition were performed to assess reproducibility. The true fracture strain is here defined as $\varepsilon_f = ln\left(\frac{A_o}{A_f}\right)$, where A_o is the initial area and A_f is the final area at fracture.

Nitric acid mass loss test (NAMLT) was carried out to determine the susceptibility to IGC following ASTM-G67 standard [31]. The corrosion test (CT) samples of dimension 50 mm × 6 mm × 4.7 mm were extracted by micro-cutting with the 50 mm dimension along the rolling direction followed by standard polishing with SiC paper (#600 grit). The cross sections of corrosion test samples were examined by optical microscopy. The polished specimens were etched using Keller etchant to observe the grain structure after corrosion.

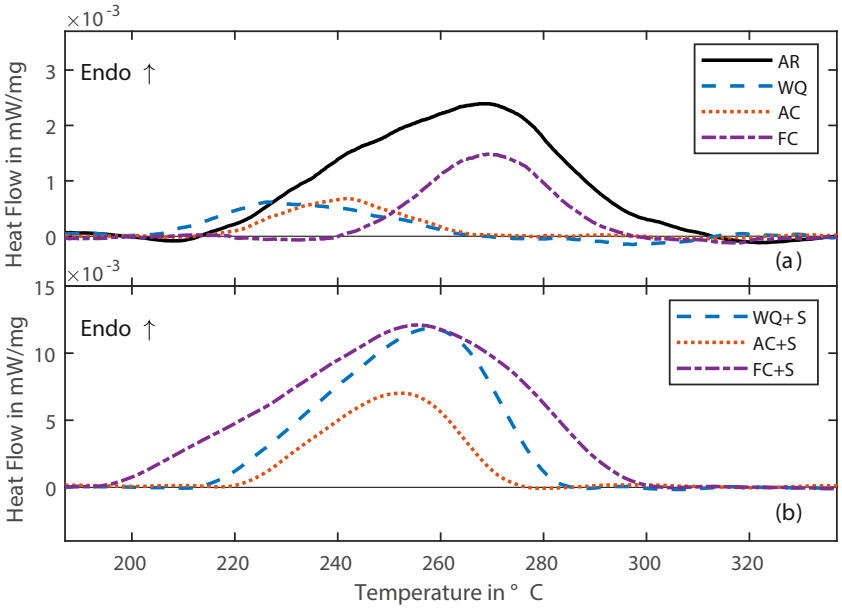

Fig. 3. DSC heating curves showing the β phase endothermic dissolution peaks for (a) non-sensitized conditions and (b) sensitized conditions. Note the difference in scale between Figures (a) and (b) required by the much larger peak observed for the sensitized samples.

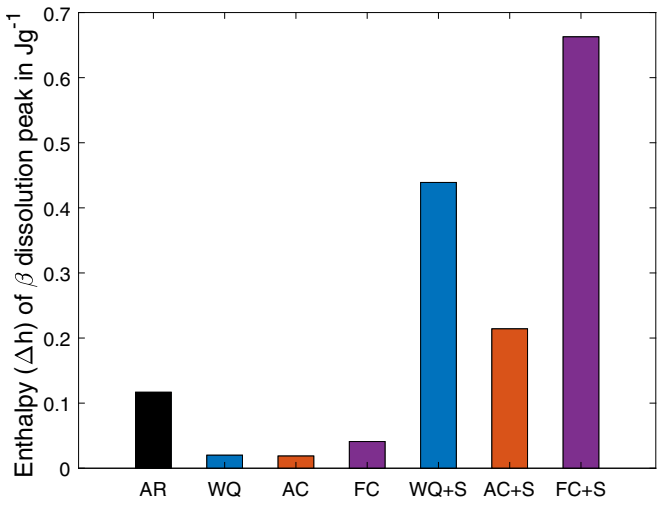

Fig. 4. Enthalpy of the β dissolution peak which is proportional to the volume fraction of β precipitates for the various heat treatment conditions.

3. Results

3.1. Microstructure observation

3.1.1. Coarse intermetallic phases

A SEM micrograph of the as received (AR) alloy 5028-H116 is shown in Fig. 2. The EDX maps shows the presence of Mn and Si rich intermetallics in the aluminum matrix. Similar SEM observations were carried out for heat treated and sensitized conditions and no significant difference in these intermetallics distribution and size was found. These intermetallics were aligned mostly along the longitudinal rolling direction.

3.1.2. β precipitation

The amount of β (Al_3Mg_2) precipitates formed in 5028- H116AA can be identified by DSC for various heat treatments. Fig. 3 shows the DSC responses of non-sensitized and sensitized alloy (see supplementary Fig. S1 for the full curve). The analysis is carried out only on the heating DSC curves, as our focus is on the identification of pre-existing phases. The endothermic peak observed around 280–300 °C is attributed to β phase dissolution, following Ref. [7, 27].

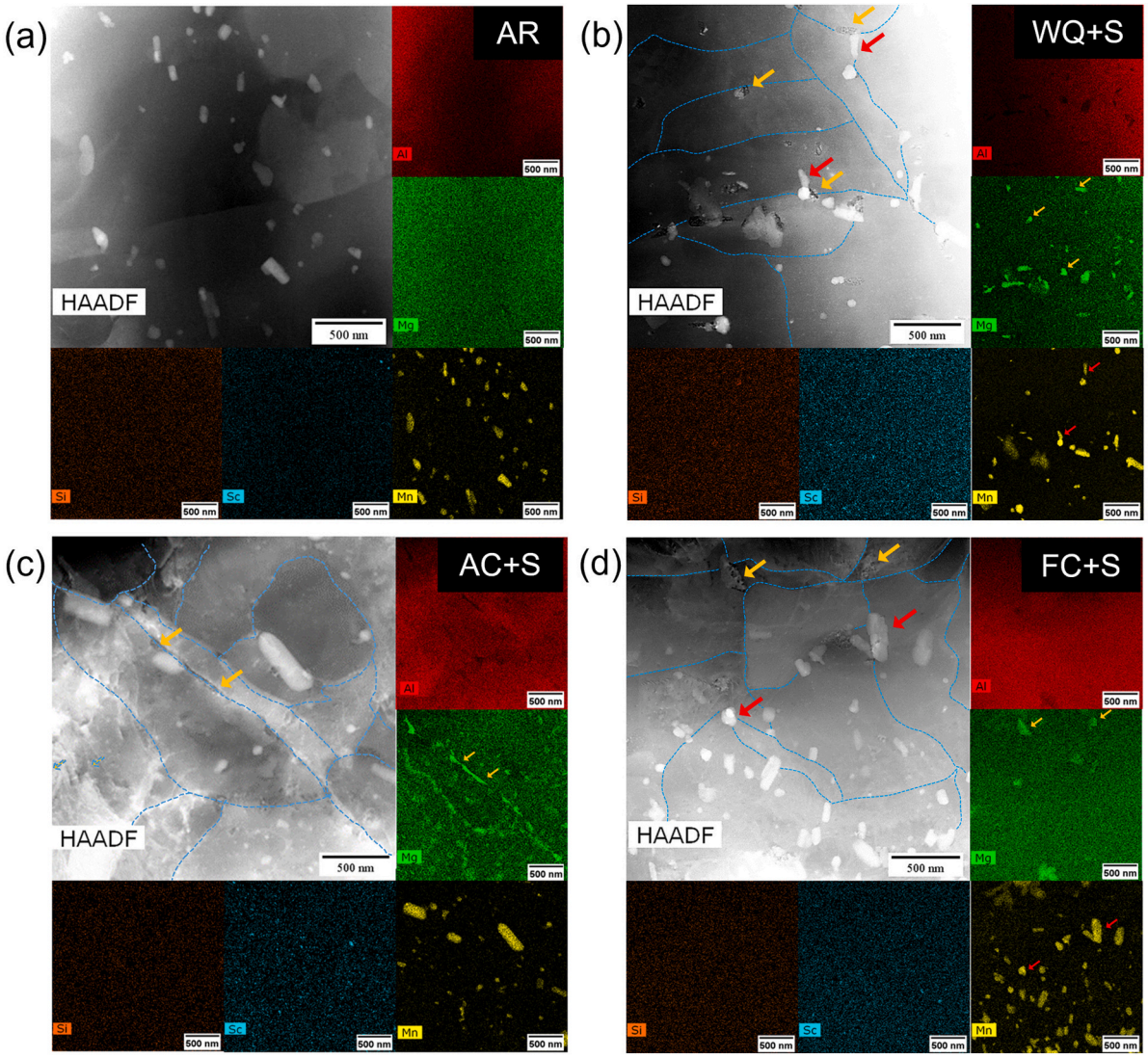

Fig. 5. STEM images with associated EDX elemental maps showing the alloying element distribution in (a) AR (b) WQ+S (c) AC+S (d) FC+S of 5028-H116 aluminum alloy (blue lines highlight grain boundaries, yellow arrows highlight β precipitate, and red arrows highlight Mn-rich dispersoids). (For interpretation of the references to colour in this figure legend, the reader is referred to the web version of this article.)

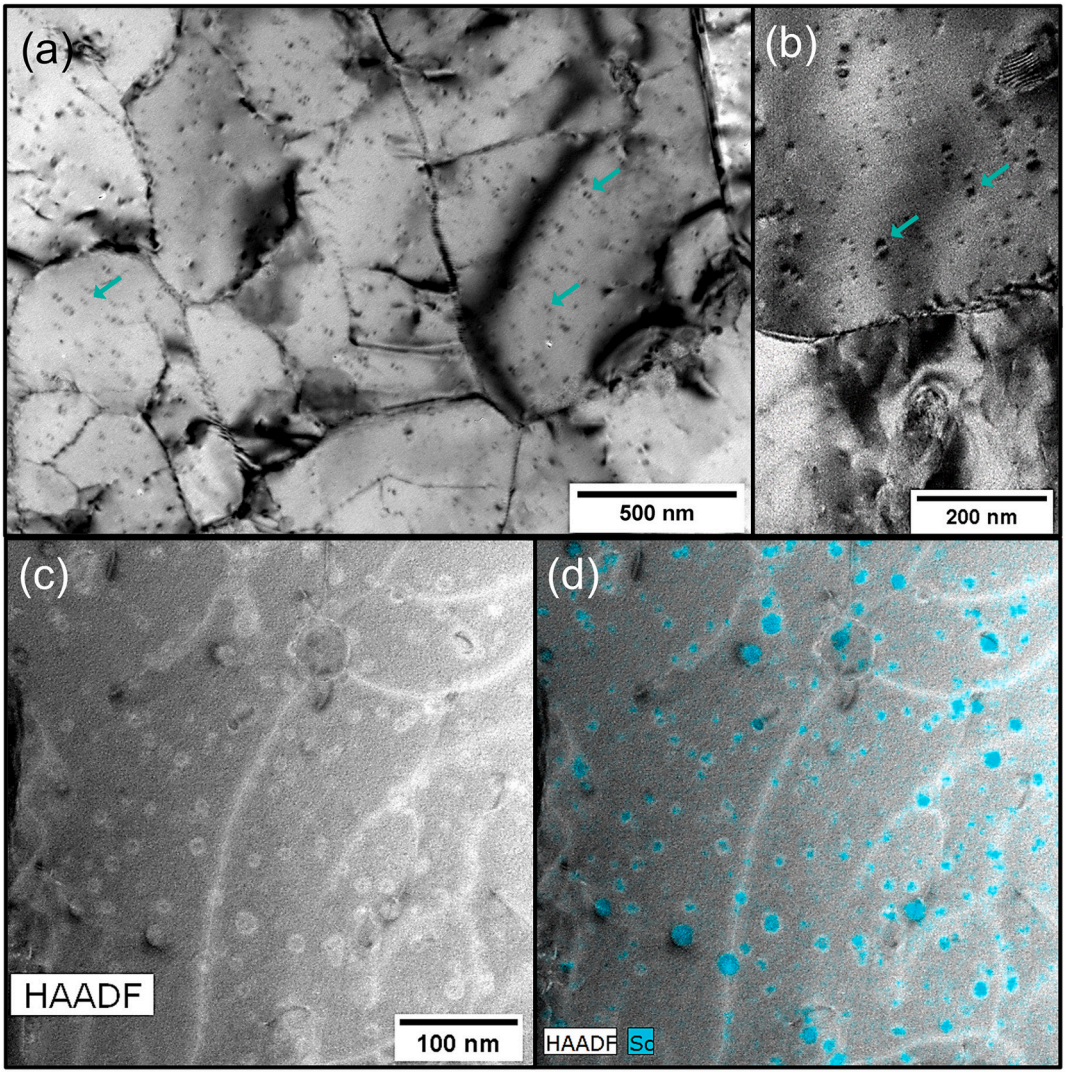

Fig. 6. (a) TEM images showing the presence of Al_3Sc precipitates in WQ+S condition (b) higher magnification TEM image showing Al_3Sc precipitates, (c) HAADF-STEM image in WQ+S condition and (d) shows STEM image in (c) overlaid with Sc enriched precipitates.

Fig. 3 shows that the β dissolution peak is varying with respect to the heat treatment conditions. In general, the area under the dissolution peak indicates the volume fraction of pre-existing phases [28]. Thus, the area under the β dissolution peak (Fig. 4) is proportional to the volume fraction of β precipitates in the heat-treated conditions. Observing the non-sensitized conditions, the volume fraction of β precipitates is larger in the AR alloy compared to WQ, AC and FC conditions. Among WQ, AC and FC conditions, an increase in cooling rate decreases the volume fraction of β precipitates. Now, the overall volume fraction of β precipitates after the 325 °C heat treatment is much lower than after the sensitization treatment. The cooling rate dependency of the volume fraction of β precipitates post sensitization is more significant. The FC+S condition presents the highest volume fraction of β precipitates followed by the WQ+S and finally AC+S condition. Here, the effect of the heat treatment cooling rate is thus not monotonous.

To clarify this difference in β (Al_3Mg_2) precipitation among the sensitized conditions (Fig. 4), HAADF-STEM imaging was carried out to determine the actual distribution of Mg rich β phase precipitates. The STEM micrographs are shown in Fig. 5 for AR and sensitized (WQ+S, AC+S, FC+S) conditions. EDX elemental maps showing the distribution of Al, Mg, Mn, Sc and Si are also provided. In Fig. 5, the EDX map confirms the presence of β precipitates that appear as sparingly distributed Mg-rich clusters. In addition, small Mn-rich intermetallics can be observed in the matrix. The distribution of Sc is not evident in Fig. 5. Fig. 6(a-b) show dispersed Sc-rich precipitates that appear in the form of kidney structure or as pair of coffee beans. These typical structures were reported previously by Yin et al. [32] and are expected to be Al_3Sc precipitates [33]. Further STEM-EDX mapping was performed at higher magnification to reveal the Sc enrichment as shown in Fig. 6(c-d).

In WQ+S condition (Fig. 5b), thick β phase precipitates can be observed along grain boundaries and inside grains (yellow arrow in Fig. 5b). These precipitates are located adjacent to Mn-rich intermetallics and are rarely independent of Mn intermetallics (red arrow in Fig. 5b). In AC+S (Fig. 5c) condition, thin elongated β phase precipitates are formed at grain boundaries as observed in the Mg map. In FC+S condition (Fig. 5d), the β precipitates are much larger and are found mostly at GB triple junctions.

Fig. 7 quantifies the nearest neighbor distance (NND) of β precipitates as a function of occurrence in different heat treatment condition computed from the TEM images. In the AR condition, the β precipitates are observed at a neighboring distance larger than 0.6 μm and even mostly higher than 2 μm from each other. Among sensitized alloys, in the AC+S, β precipitates are found typically at a NND lower than 0.2 μm, while in the WQ+S condition the NND ranges generally between 0.2 and 0.4 μm which are both close to a continuous arrangement of β precipitates. Whereas in FC+S sample the precipitates are

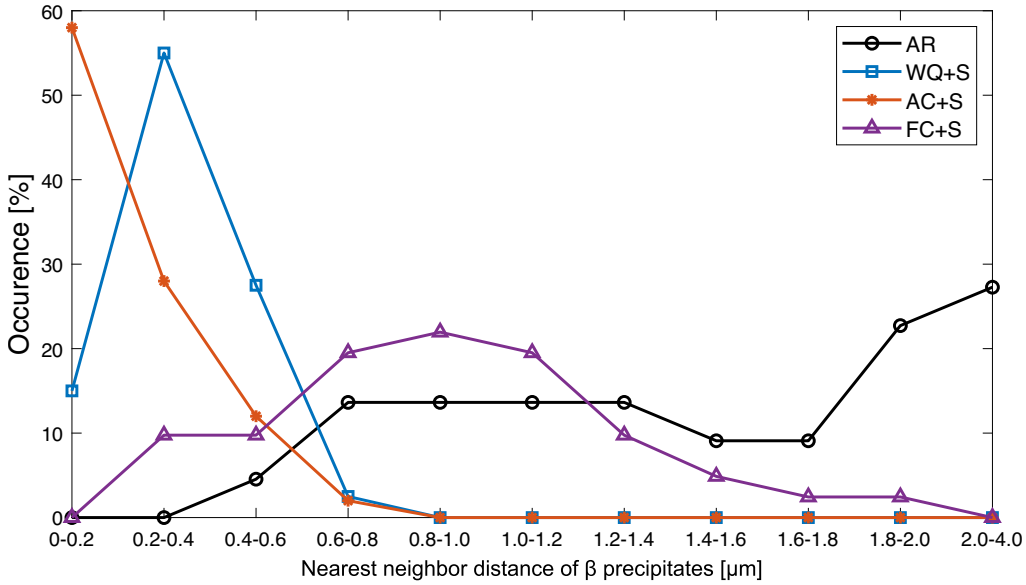

Fig. 7. 2D Distribution of nearest neighbor distance (NND) in different heat treated condition extracted from TEM images. The "occurrence" is calculated as the ratio of population in the group divided by the total number of measurements for each heat treated condition.

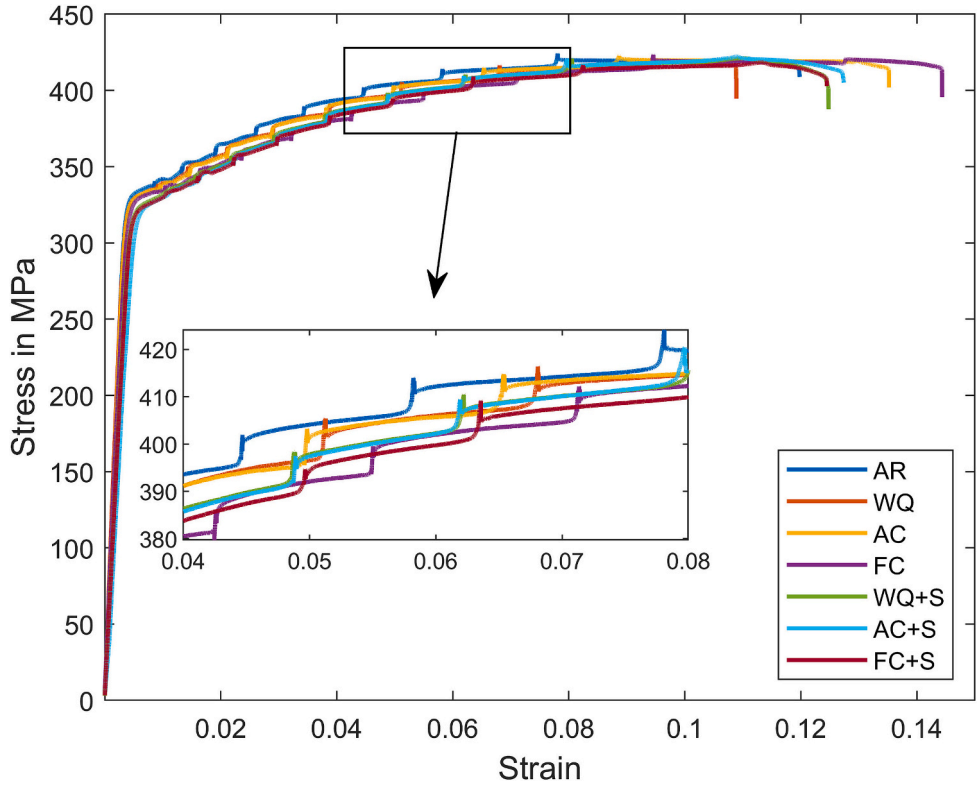

Fig. 8. Uniaxial tensile test stress-strain curves of AR and different heat treated 5028-H116 Al alloy highlighting the PLC serrations in the sub-figure.

distributed far away from each other mostly between 0.6 and 1.2 μm, hence the largest spacing between β precipitates among all sensitized conditions (WQ+S, AC+S, FC+S).

3.2. Mechanical properties

Tensile and micro-hardness (see supplementary Fig. S2) tests were conducted to study the effect of thermal treatment and cooling rate on the mechanical behavior of the 5028-H116 Al alloy. Uniaxial tensile test responses are shown in Fig. 8 for the as received (AR), heat treated and sensitized conditions. The tensile stress-strain curves (Fig. 8) exhibit stress serrations which are generally observed in Al-Mg alloys and correspond to the Portevin–Le Chatelier (PLC) effect (see supplementary Fig. S3 for individual plots). Fig. 9 reports the corresponding ultimate tensile strength, yield stress and fracture strain. The variation in the tensile strength among AR, heat treated (WQ, AC, FC) and sensitized (WQ+S, AC+S, FC+S) conditions is <1%. Whereas the yield stress is reduced by about 1.2% among heat treated (WQ, AC, FC) conditions

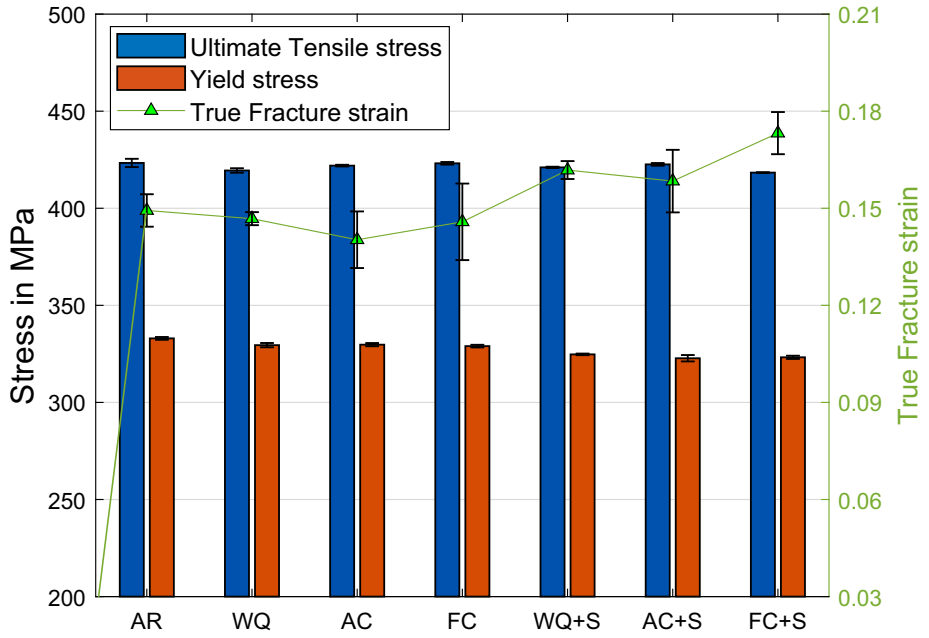

Fig. 9. Ultimate tensile strength, yield stress and true fracture strain of AR, heat treated materials following different cooling rates and sensitized thermal treatments. Error bars are systematically provided.

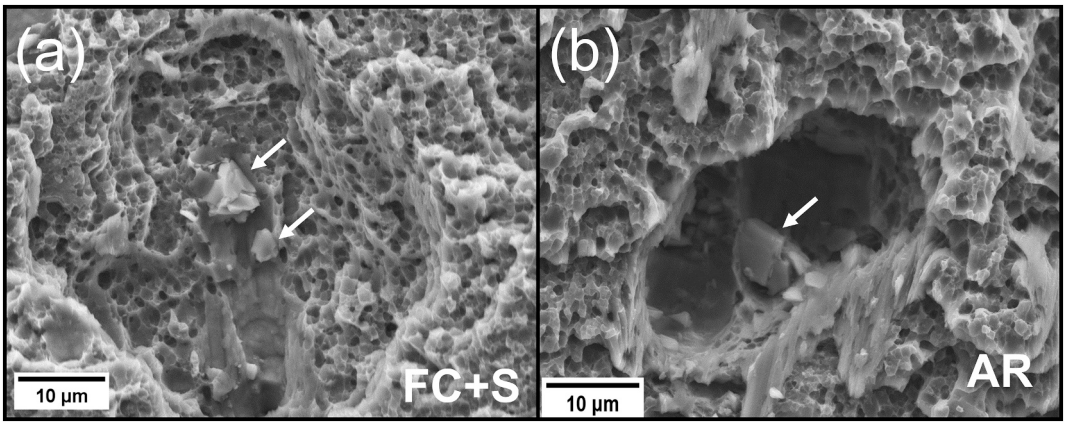

Fig. 10. Fracture surface of (a) FC + S and (b) AR condition. The white arrows points to the Mn rich intermetallic that expectedly lead to the nucleation of a large void.

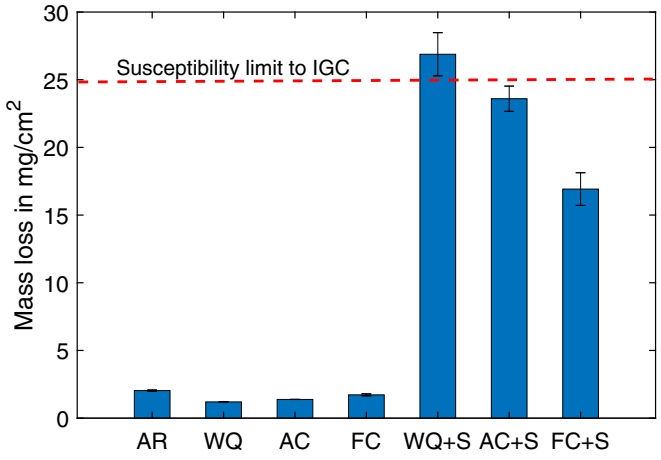

Fig. 11. Nitric acid mass loss test [NAMLT] results for different heat treatment conditions of 5028-H116 Al alloy.

compared to AR material and about 3.0% for sensitized (WQ+S, AC+S, FC+S) specimens. The micro-hardness is identical in all conditions (~117 HV) within the error of the measurement (see supplementary Fig. S2).

Fig. 10 shows fracture surfaces of tensile specimens of the two extreme conditions (FC+S and AR) featuring two populations of void sizes. Ductile shear fracture is caused by the nucleation and growth of larger voids caused by fracture or decohesion of the large intermetallics. This can be identified by the intermetallic indicated by the white arrows in Fig. 10. Now, final void coalescence seems to be triggered by a secondary population of sub-micron sized cavities visible throughout the fracture surface. These cavities are expectedly initiating on β precipitates based on the cavity size. The fracture surface among AR, heat treated (WQ, AC, FC) and sensitized (WQ+S, AC+S, FC+S) conditions do not evidence any clear difference in damage mechanism.

3.3. Corrosion resistance

The NAMLT corrosion test mass loss results are provided in Fig. 11. It shows that the AR 5028-H116 and annealed conditions (WQ, AC, FC)

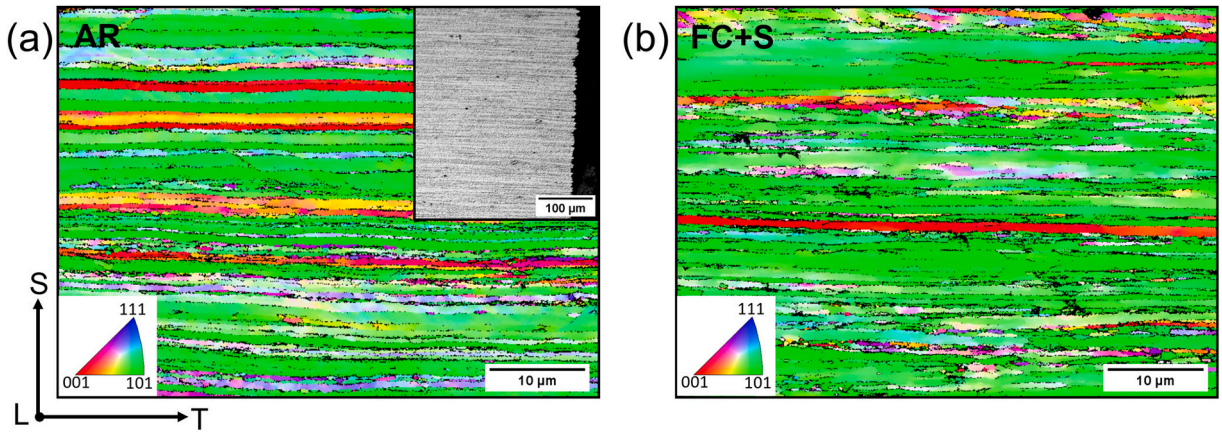

Fig. 12. EBSD IPF map providing the grains texture along S-T plane (a) AR condition, Inset: AR corroded sample indicating corrosion damage and etched to visualize grain orientation. (b) FC+S condition.

with different cooling rates involve mass losses below 3 mg/cm^2, indicating a high resistance to intergranular corrosion (IGC <25 mg/cm2) [31]. In general, annealing at 325 °C (WQ, AC, FC) leads to a slight mass loss reduction compared to that of AR 5028-H116. Conversely, the sensitization of these annealed materials (WQ+S, AC+S, FC+S) shows a significant increase in mass loss. In addition, Fig. 11 shows significant impact of the cooling rate on sensitized conditions. Among the sensitized conditions the mass loss of WQ+S specimen is over the standard limit of susceptibility to IGC [31], while AC+S condition is rather close to the susceptibility limit and FC+S condition presents a higher resistance to IGC.

The corrosion mechanism can be better understood by looking at the grain morphology. EBSD maps of Fig. 12a and b represent the elongated grains in the short transverse (S-T) plane of the two extreme conditions: AR and FC+S. No grain growth could be evidenced following the heat treatment at 325 °C and sensitization (compare FC+S condition to AR condition in Fig. 12). Fig. 12a (inset) and 13 show the cross-sectional view of the corrosion test samples along the S-T plane. The AR (Fig. 12a-inset) and annealed conditions (WQ, AC, FC) (Fig. 13 a,b,c) did not exhibit any noticeable corrosion damage. On the contrary, significant corrosion penetration cracks are observed in the sensitized conditions (WQ+S, AC+S, FC+S), see Fig. 13 d,e,f. Comparing these results with the grain structure (Fig. 12 a,b), the corrosion damage pattern confirms that IGC is the dominant corrosion mechanism occurring in the heat treated 5028-H116 Al alloy. The IGC appearance in rolled alloys significantly depends on the grain morphology with an elongation in the rolling direction [34]. Thus, the corrosion penetration depth was quantified along the Longitudinal (L), Transverse (T) and Short-transverse (S) directions and is presented in Fig. 13g. The corrosion penetration indicates the corrosion rate, which is found to be severe along L direction, slightly less severe along the T direction and minimum along the S direction. This is particularly visible in the sensitized conditions.

4. Discussion

The tensile test results (Fig. 9) do not indicate any significant variation of tensile strength due to heat treatment at 325 °C and cooling rate nor due to sensitization. This could be directly linked to the role of Al_3Sc precipitates present in the heat treated 5028 Al alloy (Fig. 6). In addition, non-recrystallized submicron grains observed in Fig. 12 explain stable mechanical properties. In general, the formation of β-phase (Al_3Mg_2) precipitates in Al-Mg alloys is known to reduce the strength of the alloy when heat treated [18]. This effect is not observed in our study, due to the formation of dominating Al_3Sc strengthening precipitates, see also Kendig et al. [24]. Jambu et al. [4] concluded that the thermally stable Al_3Sc precipitates [35] are the reason for the thermal stability of the 5024 aluminum alloy strength. Xu et al. [36] also showed that Al_3Sc precipitates are highly stable and coherent in Al-Mg-Sc alloys when annealed at 300–450 °C for up to 168 h.

In addition, the tensile curves (Fig. 8) exhibit characteristic increases and drops in flow stress. This behavior has already been observed in the Al-Mg-Sc alloy by Mogucheva et al. [37] and was associated to the dispersed Al_3Sc precipitates which pin the gliding dislocations. Their unpinning at higher stress leads to these sudden stress jumps. The observed serrations are identical in all conditions (Fig. 8) and have been attributed to A-type serrations, see Zhang et al. [38] for additional details. A change in the pattern of serrations is generally observed when there is a change in the testing temperature, applied strain or a difference in grain morphology [38]. As our EBSD measurements (Fig. 12) do not highlight any difference in grain morphology and size after the 325 °C heat treatment and, as similar testing conditions (temperature and strain rate) were applied, identical serration patterns are expected to be observed. The β phase precipitates do not either seem to influence the stress flow in this new 5028 aluminum alloy.

The sensitization heat treated conditions lead to some increased fracture strain (Fig. 9) when compared to the equivalent non-sensitized condition. Sensitization treatment promotes the formation of a higher volume fraction of β (Al_3Mg_2) precipitates as concluded from the DSC results (Fig. 4). Thus, the small increase in fracture strain is possibly due to the interaction of dislocations with β (Al_3Mg_2) precipitates as well as with the Al_3Sc precipitates. In this context, it is worth noticing that the Sc-enriched precipitates are preferentially seen on or around dislocations (Fig. 6 (c-d)). The pinning of dislocations and sub-grain boundaries on the Sc rich precipitates has been reported by Liu et al. [39]. Overall, no significant effect of the heat treatment is observed on the mechanical properties.

Concerning the corrosion behavior, the mass loss (Fig. 11) shows the same trend as the IGC penetration depth (Fig. 13). Lim et al. [34] showed that corrosion in Al-Mg alloys occurs along the GB and once the complete GB is corroded, the grain falls out in the wake leading to a pit at the surface. The reduction of mass loss in the annealed condition (WQ, AC, or FC) compared to that of AR 5028-H116 can be attributed to the dissolution of pre-existing β phase precipitates when annealed at 325 °C. Consequently, the volume fraction of β phase precipitates in annealed conditions (WQ, AC, FC) is lower than in the AR 5028 Al alloy (Fig. 4) delaying corrosion. The significant increase in volume fraction of β precipitates after the sensitization heat treatment (Fig. 4) is related to the lower corrosion resistance reported in Fig. 11.

Table 2 summarizes the results of the observations made in Section 3 and will help the reader to follow the discussion that comes afterwards.

The significant effect of cooling rate on the corrosion resistance of

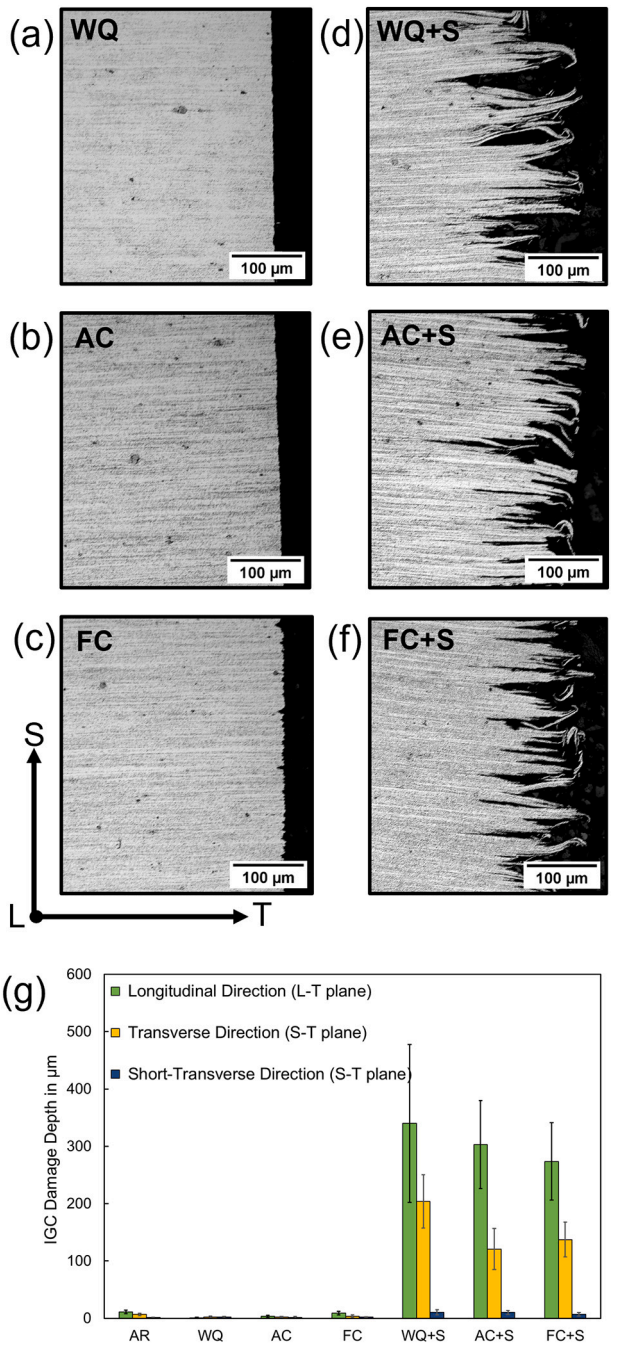

Fig. 13. Heat treated 5028-H116 corroded samples indicating corrosion damage in the S-T plane and etched to visualize grain orientation for various heat treatment conditions: (a) water quenched [WQ], (b) air cooled [AC], (c) furnace cooled [FC], (d) water quenched and sensitized [WQ+S], (e) air cooled and sensitized [AC+S], (f) furnace cooled and sensitized [FC+S]. (g) IGC Corrosion damage depth quantified in Longitudinal, Transverse and Short-Transverse direction for the various heat-treated conditions of 5028-H116 alloy.

sensitized samples (WQ+S, AC+S, FC+S) is evident in Fig. 11. The general trend shows that an increase in cooling rate after annealing at 325 °C increases the IGC (Table 2). For the WQ+S and AC+S conditions, IGC susceptibility (Fig. 13) can be directly related to their volume fraction of β precipitates. Now, the FC+S condition presents the lowest susceptibility to IGC among all sensitized conditions (Figs. 11 and 13). Unexpectedly, that condition also holds the highest volume fraction of β precipitates among all sensitized conditions (WQ+S, AC+S, FC+S) (Table 2). This apparent inconsistency leads to the proposition that a

Table 2
Summary of experimental results for different heat treatment conditions on the 5028-H116 Al alloy.

Specimen	Corrosion mass loss [mg/cm^2]	DSC area proportional to volume fraction of β precipitates [J/g]	Nearest neighbor distance of β precipitates [nm]	Thickness of β precipitates [nm]
WQ+S	26.8 ± 1.5	0.44	340 ± 118	50 ± 21
AC+S	23.6 ± 0.9	0.21	230 ± 136	41 ± 19
FC + S	16.9 ± 1.2	0.67	902 ± 364	111 ± 44

higher volume fraction of β phase precipitates does not systematically exhibit higher susceptibility to IGC. The precipitate distribution plays a major role on its susceptibility to corrosion.

The nucleation sites of β phase precipitation are known to be heterogeneous. The cooling rate shows clear effects on β precipitates distribution in sensitized condition by their nucleation on Mn dispersoids, grain boundaries or triple junctions with decreasing cooling rate, as evidenced by the TEM results of Fig. 5. Ding et al. [40] explained the transition of β precipitates nucleation sites at 220 °C from GB to triple junction using classical nucleation theory in 5083 Al alloy containing erbium and zirconium. According to their study, the nucleation rate at GB triple junctions is 10 times higher than at the GB at 220 °C. At a lower temperature (100–150 °C), the nucleation rate is 100 times higher at GB than at GB triple junctions. This can be related to the TEM observations in Fig. 5 for the FC+S condition, where the β precipitates nucleate at GB triple junctions during the furnace cooling (FC) and grow during sensitization. Similarly, for the AC+S sample the air-cooling curve (Fig. 1) exhibits a slight reduction in cooling rate at around 170 °C and below, leading to a higher nucleation rate of β precipitates at grain boundaries in AC+S condition (Fig. 5c). Zhu et al. [41] found Mn rich intermetallics are low energy barrier sites for β precipitate nucleation at low temperature. It is the case for WQ+S condition when subjected to sensitization, see Fig. 5b. Hence, as a summary, the rate of β precipitate nucleation at different nucleation sites is a function of temperature. The change in temperature due to different cooling rates led to a shift of nucleation sites towards lower energy sites.

During sensitization, Mg atoms diffuse towards pre-existing β precipitates as the nucleation at lower temperature requires higher energy. Thus, the growth of β precipitates is favored at the detriment of their nucleation in AC+S and FC+S samples [14,42]. The phenomenon of quenched-in vacancies explains the role of trapped vacancies due to rapid cooling from high temperature [43]. These vacancies then migrate to lower nucleation energy sites, e.g. the edges of the Mn dispersoids. This then drives the precipitate nucleation and growth during sensitization in the WQ+S sample.

The perfect continuity of β phase precipitates is known to be crucial for IGC in sensitized Al-Mg alloys [6,10]. Continuous β phase precipitates increase IGC rate due to uninterrupted difference in corrosion potential. Among sensitized conditions, the AC+S condition exhibits continuous thin β phase precipitates along the GB (see Table 2 and Fig. 5c). The WQ+S condition exhibits rather continuous thick β phase precipitates along GBs adjacent to Mn dispersoids (see Table 2 and Fig. 5b). The WQ+S condition displays a higher mass loss as the IGC penetration depth is larger in the WQ+S sample compared to the AC+S sample. This suggests that the rather continuous thick β precipitates of higher volume fraction (sample WQ+S, see Table 2) are more vulnerable to corrosion than continuous thin β precipitates with a lower volume fraction of β precipitates (sample AC+S, see Table 2). Whereas, in the FC+S condition the β precipitates are formed at GB triple junction (Fig. 5d) which are far apart from each other compared to AC+S and WQ+S conditions (Fig. 7), this significantly reduces the local corrosion potential along GB favoring a better resistance to corrosion of the FC+S condition compared to all other sensitized conditions. To summarize, the main difference in β precipitate distribution causing the better

corrosion resistance of the FC+S sample is actually associated to the precipitate inter-distance.

5. Conclusion

The influence of cooling rate during heat treatments on the mechanical and corrosion properties of aluminum alloy 5028-H116 was investigated. The annealing at 325 °C followed by sensitization heat treatment at 120 °C for 7 days did not significantly affect the strength of the alloy. The low fracture strain of the alloy is slightly increased by the annealing and sensitization heat treatment which is proposed to be due to a larger β (Al_3Mg_2) precipitates volume fraction. But, overall, this effect is rather limited. On the contrary, the sensitization heat treatment significantly increases the corrosion mass loss of 5028-H116 aluminum alloy. The main findings of this study are:

1. The cooling rate after this 325 °C heat treatment has a significant impact on the site of nucleation and growth of β (Al_3Mg_2) precipitate during the following sensitization heat treatment.
2. The β (Al_3Mg_2) precipitate distribution critically affects intergranular corrosion (IGC) in addition to the better known effect of β (Al_3Mg_2) volume fraction.
3. The IGC rate can be decelerated by nucleating the β (Al_3Mg_2) phase precipitates at triple junction GB using slow (furnace) cooling after the 325 °C annealing treatment.

Thus, this study has demonstrated that implementing slow (furnace) cooling after annealing 5028-H116 at 325 °C is advantageous in increasing the resistance to IGC after a sensitization heat treatment.

Declaration of Competing Interest

The authors declare that they have no known competing financial interests or personal relationships that could have appeared to influence the work reported in this paper.

Data availability

Data will be made available on request.

Acknowledgements

Novelis is acknowledged for providing the material and for technical support.

Appendix A. Supplementary data

Supplementary data to this article can be found online at https://doi.org/10.1016/j.matchar.2023.112886.

References

[1] N.V. Eremeev, P.Y. Predko, V.V. Eremeev, A.V. Bespalov, S.G. Bochvar, Technological aspects of thin plate production for aircraft construction based on Al–Mg–Sc alloys, Inorg. Mater. Appl. Res. 12 (2) (2021) 288–295, https://doi.org/10.1134/S2075113321020131.
[2] V.K. Mann, A.Y. Krokhin, A.N. Alabin, V.F. Frolov, I.A. Redkin, R.O. Vahromov, Al-Mg-Sc alloys for sheet, plate, and additive manufacturing for automotive and aerospace, Light Metal Age 74 (5) (2016) 12–16. Retrieved from, https://elibrary.ru/item.asp?id=29551799. Retrieved from.
[3] F. Zimmermann, A. Brosius, R.E. Beyer, J. Standfuß, A. Jahn, D. Banke, Creep forming of very thin AlMgSc sheets for aeronautical applications, in: Procedia Manufacturing vol. 15, Elsevier, 2018, pp. 1008–1015, https://doi.org/10.1016/j.promfg.2018.07.393.
[4] S. Jambu, B. Lenczowski, R.J.K. Rauh, Creep forming of AlMgSc alloys for aeronautic and space applications, in: Proceedings of the 23rd International Congress of Aeronautical Sciences, 2002.
[5] M. Vorel, S. Hinsch, M. Konopka, M. Scheerer, AlMgSc alloy 5028 status of maturation, in: 7Th European Conference for Aeronautics and Space Sciences (Eucass), 2017, https://doi.org/10.13009/EUCASS2017-633.
[6] R. Zhang, S.P. Knight, R.L. Holtz, R. Goswami, C.H.J. Davies, N. Birbilis, A survey of sensitization in 5xxx series aluminum alloys, in: Corrosion vol. 72, 2016, pp. 144–159, https://doi.org/10.5006/1787.
[7] M.J. Starink, A.M. Zahra, β' and β precipitation in an Al-Mg alloy studied by DSC and TEM, Acta Mater. 46 (10) (1998) 3381–3397, https://doi.org/10.1016/S1359-6454(98)00053-6.
[8] D. Scotto D'Antuono, β Phase Growth and Precipitation in the 5xxx Series Aluminum Alloy System, Ph. D. Thesis., Drexel University, 2017.
[9] R. Goswami, G. Spanos, P.S. Pao, R.L. Holtz, Precipitation behavior of the ß phase in Al-5083, Mater. Sci. Eng. A 527 (4–5) (2010) 1089–1095, https://doi.org/10.1016/j.msea.2009.10.007.
[10] G. Yi, D.A. Cullen, K.C. Littrell, W. Golumbfskie, E. Sundberg, M.L. Free, Characterization of Al-Mg alloy aged at low temperatures, Metallurg. Mater. Trans. A Phys. Metallurg. Mater. Sci. 48 (4) (2017) 2040–2050, https://doi.org/10.1007/s11661-017-3992-2.
[11] J. Yan, N.M. Heckman, L. Velasco, A.M. Hodge, Improve sensitization and corrosion resistance of an Al-Mg alloy by optimization of grain boundaries, Sci. Rep. 6 (2016), https://doi.org/10.1038/srep26870.
[12] D. Scotto D'Antuono, J. Gaies, W. Golumbfskie, M.L. Taheri, Direct measurement of the effect of cold rolling on β phase precipitation kinetics in 5xxx series aluminum alloys, Acta Mater. 123 (2017) 264–271, https://doi.org/10.1016/j.actamat.2016.10.060.
[13] J. Desai Choundraj, J. Kacher, Influence of misorientation angle and local dislocation density on β-phase distribution in Al 5xxx alloys, Sci. Rep. 12 (1) (2022) 1–8, https://doi.org/10.1038/s41598-022-05948-8.
[14] R.C. Picu, D. Zhang, Atomistic study of pipe diffusion in Al-Mg alloys, Acta Mater. 52 (1) (2004) 161–171, https://doi.org/10.1016/j.actamat.2003.09.002.
[15] N. Birbilis, R.G. Buchheit, Electrochemical characteristics of intermetallic phases in aluminum alloys, J. Electrochem. Soc. 152 (4) (2005) B140, https://doi.org/10.1149/1.1869984.
[16] C.T. Wu, S.L. Lee, Y.F. Chen, H.Y. Bor, K.H. Liu, Effects of Mn, Zn additions and cooling rate on mechanical and corrosion properties of Al-4.6Mg casting alloys, Materials 13 (8) (2020), https://doi.org/10.3390/MA13081983.
[17] R. Zhang, R.K. Gupta, C.H.J. Davies, A.M. Hodge, M. Tort, K. Xia, N. Birbilis, The influence of grain size and grain orientation on sensitization in AA5083, Corrosion 72 (2) (2016) 160–168, https://doi.org/10.5006/1703.
[18] W. Wen, Y. Zhao, J.G. Morris, The effect of Mg precipitation on the mechanical properties of 5xxx aluminum alloys, Mater. Sci. Eng. A 392 (1–2) (2005) 136–144, https://doi.org/10.1016/j.msea.2004.09.059.
[19] T. Dorin, M. Ramajayam, A. Vahid, T. Langan, Aluminium scandium alloys, in: Fundamentals of Aluminium Metallurgy, 2018, pp. 439–494, https://doi.org/10.1016/b978-0-08-102063-0.00012-6.
[20] J.Y. Zhang, Y.H. Gao, C. Yang, P. Zhang, J. Kuang, G. Liu, J. Sun, Microalloying Al alloys with Sc: a review, Rare Metals (2020, June 1), https://doi.org/10.1007/s12598-020-01433-1. University of Science and Technology Beijing.
[21] M. Jia Li, S. Liu, X. Dong Wang, Y. Jia Shi, Q. Lin Pan, X. Jie Zhou, N. Birbilis, Improved intergranular corrosion resistance of Al-Mg-Mn alloys with Sc and Zr additions, Micron 154 (2022), 103202, https://doi.org/10.1016/j.micron.2021.103202.
[22] Y.A. Filatov, V.I. Yelagin, V.V. Zakharov, New Al-Mg-Sc alloys, Mater. Sci. Eng. A 280 (1) (2000) 97–101, https://doi.org/10.1016/S0921-5093(99)00673-5.
[23] Z. Tang, F. Jiang, M. Long, J. Jiang, H. Liu, M. Tong, Effect of annealing temperature on microstructure, mechanical properties and corrosion behavior of Al-Mg-Mn-Sc-Zr alloy, Appl. Surf. Sci. 514 (2020), https://doi.org/10.1016/j.apsusc.2020.146081.
[24] K.L. Kendig, D.B. Miracle, Strengthening mechanisms of an Al-Mg-Sc-Zr alloy, Acta Mater. 50 (16) (2002) 4165–4175, https://doi.org/10.1016/S1359-6454(02)00258-6.
[25] Y. Deng, G. Xu, Z. Yin, X. Lei, J. Huang, Effects of Sc and Zr microalloying additions on the recrystallization texture and mechanism of Al–Zn–Mg alloys, J. Alloys Compd. 580 (2013) 412–426, https://doi.org/10.1016/j.jallcom.2013.06.020.
[26] R. Braun, Effect of thermal exposure on the microstructure, tensile properties and the corrosion behaviour of 6061 aluminium alloy sheet, Mater. Corros. 56 (3) (2005) 159–165, https://doi.org/10.1002/maco.200403825.
[27] S. Nebti, D. Hamana, G. Cizeron, Calorimetric study of pre-precipitation and precipitation in Al-Mg alloy, Acta Metall. Mater. 43 (9) (1995) 3583–3588, https://doi.org/10.1016/0956-7151(95)00023-O.
[28] B. Milkereit, M.J. Starink, P.A. Rometsch, C. Schick, O. Kessler, Review of the quench sensitivity of aluminium alloys: analysis of the kinetics and nature of quench-induced precipitation, Materials 12 (24) (2019), https://doi.org/10.3390/MA12244083.
[29] ISO, ISO 6507-1:2005: Metallic materials – Vickers hardness test – Part 1: Test method, ISO, 2005. Retrieved from, https://www.iso.org/obp/ui/#iso:std:iso:6507:-1:ed-4:v1:en.
[30] ASTM E8, Standard Test Methods for Tension Testing of Metallic Materials vol. 16, ASTM International, 2014. Retrieved from, https://www.astm.org/e0008_e0008m-16.html.
[31] ASTM-G67, Standard Test Method for Determining the Susceptibility to Intergranular Corrosion of 5XXX Series Aluminum Alloys by Mass Loss After Exposure to Nitric Acid (NAMLT Test). Annual Book of ASTM Standards, 2004, pp. 1–5, https://doi.org/10.1520/G0067-18.
[32] Z. Yin, Q. Pan, Y. Zhang, F. Jiang, Effect of minor Sc and Zr on the microstructure and mechanical properties of Al–Mg based alloys, Mater. Sci. Eng. A 280 (1) (2000) 151–155, https://doi.org/10.1016/S0921-5093(99)00682-6.

[33] J. Xie, X.P. Chen, L. Mei, G.J. Huang, Q. Liu, Investigation of the hardening behavior during recrystallization annealing in Al-Mg-Sc alloy, J. Alloys Compd. 859 (2021), https://doi.org/10.1016/j.jallcom.2020.157807.
[34] M.L.C. Lim, J.R. Scully, R.G. Kelly, Intergranular corrosion penetration in an Al-Mg alloy as a function of electrochemical and metallurgical conditions, Corrosion 69 (1) (2013) 35–47, https://doi.org/10.5006/0722.
[35] J. Jiang, F. Jiang, M. Zhang, Z. Tang, M. Tong, Al3(Sc, Zr) precipitation in deformed Al-Mg-Mn-Sc-Zr alloy: effect of annealing temperature and dislocation density, J. Alloys Compd. 831 (2020), https://doi.org/10.1016/j.jallcom.2020.154856.
[36] P. Xu, F. Jiang, Z. Tang, N. Yan, J. Jiang, X. Xu, Y. Peng, Coarsening of Al3Sc precipitates in Al-Mg-Sc alloys, J. Alloys Compd. 781 (2019) 209–215, https://doi.org/10.1016/j.jallcom.2018.12.133.
[37] A. Mogucheva, D. Yuzbekova, R. Kaibyshev, T. Lebedkina, M. Lebyodkin, Effect of grain refinement on jerky flow in an Al-Mg-Sc alloy, Metall. Mater. Trans. A 47 (5) (2016) 2093–2106, https://doi.org/10.1007/s11661-016-3381-2.
[38] Y. Zhang, J.P. Liu, S.Y. Chen, X. Xie, P.K. Liaw, K.A. Dahmen, Y.L. Wang, Serration and noise behaviors in materials, Prog. Mater. Sci. 90 (2017) 358–460, https://doi.org/10.1016/j.pmatsci.2017.06.004.
[39] J. Liu, P. Yao, N. Zhao, C. Shi, H. Li, X. Li, S. Yang, Effect of minor Sc and Zr on recrystallization behavior and mechanical properties of novel Al-Zn-Mg-Cu alloys, J. Alloys Compd. 657 (2016) 717–725, https://doi.org/10.1016/j.jallcom.2015.10.122.
[40] Y. Ding, K. Gao, H. Huang, S. Wen, X. Wu, Z. Nie, D. Zhou, Nucleation and evolution of β phase and corresponding intergranular corrosion transition at 100–230 °C in 5083 alloy containing Er and Zr, Mater. Des. 174 (2019), 107778, https://doi.org/10.1016/J.MATDES.2019.107778.
[41] Y. Zhu, D.A. Cullen, S. Kar, M.L. Free, L.F. Allard, Evaluation of Al3Mg2 precipitates and Mn-rich phase in aluminum-magnesium alloy based on scanning transmission electron microscopy imaging, Metallurg. Mater. Trans. A Phys. Metallurg. Mater. Sci. 43 (13) (2012) 4933–4939, https://doi.org/10.1007/s11661-012-1354-7.
[42] J. Yan, A.M. Hodge, Study of β precipitation and layer structure formation in Al 5083: the role of dispersoids and grain boundaries, J. Alloys Compd. 703 (2017) 242–250, https://doi.org/10.1016/j.jallcom.2017.01.360.
[43] D.A. Porter, K.E. Easterling, M.Y. Sherif, Phase Transformations in Metals and Alloys, CRC Press, Boca Raton, 2021, pp. 297–299, https://doi.org/10.1201/9781003011804.